Supplementary Information (SI) for Journal of Materials Chemistry C.

Supplementary Information

Enhanced and Robust Room Temperature Excitonic Structures of Li-doped $CsPbBr_3$ Nanocrystals

Parisa Alimohamadi[a,*], Vipin Yadav[b,*], Yixuan Dou[c,*], Era Shehu[c], Brady J. Talbert[b], Yannick Pleimling[b], Stephen McGill[d], Brenden A. Magill[b], Lina Quan[c], Christopher J. Stanton[a,†], and Giti A. Khodaparast[b,†]
[a]Department of Physics, University of Florida, Gainesville, FL, USA.
[b]Department of Physics, Virginia Tech, Blacksburg, VA, USA.
[c]Department of Chemistry, Virginia Tech, Blacksburg, VA, USA.
[d]National High Magnetic Field Laboratory, Tallahassee, FL, USA.
[†] Corresponding authors: `khoda@vt.edu and stanton@ufl.edu`.
[*]The authors with equal contributions.

Supplementary Note

This document provides additional methods, figures, tables, and analyses that support the main manuscript, including quantitative checks such as effective-mass estimates, tail-temperature extraction, power-law scaling, and peak-energy stability, as well as complementary low-fluence spectra that support the assignments and trends discussed in the main text.

Contents

S1 Excitonic Properties

To provide a better picture of our observed room-temperature (RT) optical spectra, we adopted a simple effective-mass approach to show the exciton binding energy, Bohr radius, and quantum-confinement energy in $CsPbBr_3$. These estimates show that our nanocrystals (NCs) lie in the weak-confinement regime and that modest Li-induced size variations can produce only small shifts in the absorption edge, consistent with the discussions in the main text.

We estimate the exciton binding energy and Bohr radius in $CsPbBr_3$ NCs using the hydrogenic effective-mass approximation. We used electron and hole effective masses of $m_e = 0.134\,m_0$ and $m_h = 0.128\,m_0$ [1], where the reduced mass is $\mu = (m_e m_h)/(m_e + m_h)$. For a dielectric constant ε (scanned from 2 to 25), the binding energy and Bohr radius are given by:

$$E_{\mathrm{B}}(\varepsilon) = 13.6\ \mathrm{eV}\,\frac{\mu}{m_0}\,\frac{1}{\varepsilon^2}, \qquad a_{\mathrm{B}}^*(\varepsilon) = a_0\,\varepsilon\,\frac{m_0}{\mu}, \quad a_0 = 0.0529\ \mathrm{nm}.$$

Fig. S1(a) shows E_{B} decreasing as $1/\varepsilon^2$ and a_{B}^* increasing linearly with ε, consistent with the effective-mass picture. The quantum-confinement energy shown in **Fig. S1(b)** follows the particle-in-a-box scaling:

$$E_{\mathrm{Q}} = \frac{\pi^2\hbar^2}{2\mu L^2},$$

where L is the NC's dimension and μ is the reduced effective mass.

For optical excitation, the relevant dielectric screening is governed by the high-frequency dielectric constant ε_∞ because exciton formation and radiative recombination occur faster than full lattice polarization can respond. In $CsPbBr_3$, reported longitudinal-optical phonon energies span ~4.6-19 meV [2–4], corresponding to lattice response times of tens to hundreds of femtoseconds, so electronic screening dominates during emission.

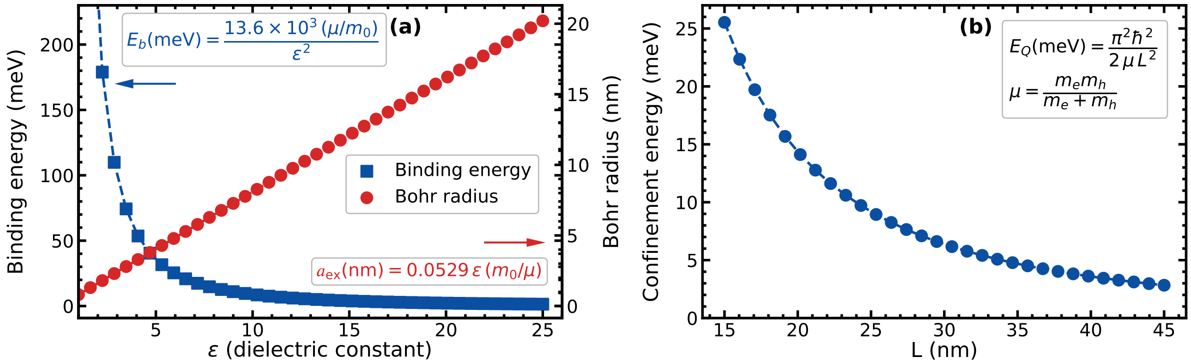

Figure S1 Excitonic and quantum-confinement properties of $CsPbBr_3$ NCs within the effective-mass and particle-in-a-box approximations. **(a)** Exciton binding energy (blue) and excitonic Bohr radius (red) as functions of the dielectric constant ε. The binding energy decreases approximately as $1/\varepsilon^2$, while the Bohr radius increases linearly with ε, reflecting reduced Coulomb attraction and enhanced spatial extension of the electron–hole pair in more polarizable media. **(b)** Quantum-confinement energy as a function of NC size L, following the expected inverse-square dependence $E_Q \propto L^{-2}$ for a particle-in-a-box model. Together, the two panels highlight the competing roles of dielectric screening and spatial confinement in determining the optical and many-body properties of perovskite NCs.

Accordingly, we adopt $\varepsilon \approx 4$–5, consistent with reported high-frequency/optical dielectric values. [5–10] Using this range with $m_e = 0.134\, m_0$ and $m_h = 0.128\, m_0$ [1], the hydrogenic model yields $E_{\mathrm{B}} \approx 35 - 55\,\mathrm{meV}$ and $a_{\mathrm{B}}^* \approx 3.2 - 4.0\,\mathrm{nm}$, consistent with reported RT values of $E_{\mathrm{B}} \approx 35 - 60\,\mathrm{meV}$. [2, 11–15]

For NC sizes of $L = 20 - 40\,\mathrm{nm}$, a particle-in-a-box estimate gives a small confinement energy $E_{\mathrm{Q}} \approx 3.6 - 14\,\mathrm{meV}$, placing the system in the weak-confinement regime ($a_{\mathrm{B}}^* \ll L$). In this regime, modest Li-induced size changes can account for only a small absorption-edge redshift while leaving the intrinsic electronic structure largely unchanged.

S2 Photo-excited Carrier Temperature: High-fluence (NHMFL)

The photoexcited carrier temperature was extracted by fitting the high-energy tail of the photoluminescence (PL) spectra for both undoped (0% Li) and Li-doped (40% Li) NCs at RT. Neglecting the density-of-states $\sqrt{E - E_g}$ prefactor, we model the tail as:

$$I(E) \;=\; C \;+\; I_0 \exp\!\left[-\frac{E - E_g}{k_B T}\right],$$

where C accounts for a small background, I_0 is a prefactor, and E_g is taken as the absorption onset energy (optical band edge) from the main text. Here, E_g is used only as a reference to define $\Delta E = E - E_g$.

Taking the logarithm yields:

$$\ln(I - C) \;=\; -\frac{1}{k_B T}(E - E_g) + \mathrm{const},$$

so that the carrier temperature can be extracted from the slope (s):

$$s \;=\; -\frac{1}{k_B T}, \qquad T \;=\; -\frac{1}{s\, k_B}.$$

The fitting is performed over the high-energy tail region, where the carrier distribution follows a quasi-thermal Boltzmann behavior. The extracted temperature, therefore, represents an effective carrier temperature rather than the lattice temperature. **Fig. S2(a)** and **Fig. S2(c)** show the high-energy-tail fits overlaid on the measured spectra, while **Fig. S2(b)** and **Fig. S2(d)** summarize the extracted carrier temperatures as a function of excitation fluence. These results quantify the evolution of the high-energy tail and provide a consistent metric for comparing carrier thermalization behavior between undoped and Li-doped samples, as reflected in the extracted effective carrier temperature.

S3 Photoluminescence Spectra: Low-fluence (Virginia Tech)

In this section, we present the low-fluence ($\mu\mathrm{J/cm^2}$) PL responses of 0% and 40% lithium-doped lead-halide perovskite NCs at RT under excitation at 800 nm. Data were measured using a Chameleon Ultra (Verdi-pumped Ti:sapphire gain medium) delivering sub-200 fs pulses. The laser repetition rate is 80 MHz, with a spot size of 0.25 mm, enabling us to probe the NCs at very low fluences on the order of $\mu\mathrm{J/cm^2}$. **Fig. S3** displays the low-fluence PL spectra at RT for both 0% and 40% Li NCs on both linear and semi-log scales. The spectra reveal several excitonic features. In contrast to the high-fluence NHMFL measurements discussed in the main text, this low-fluence regime (Virginia Tech data) probes the intrinsic excitonic response in the low-excitation regime, where state filling,

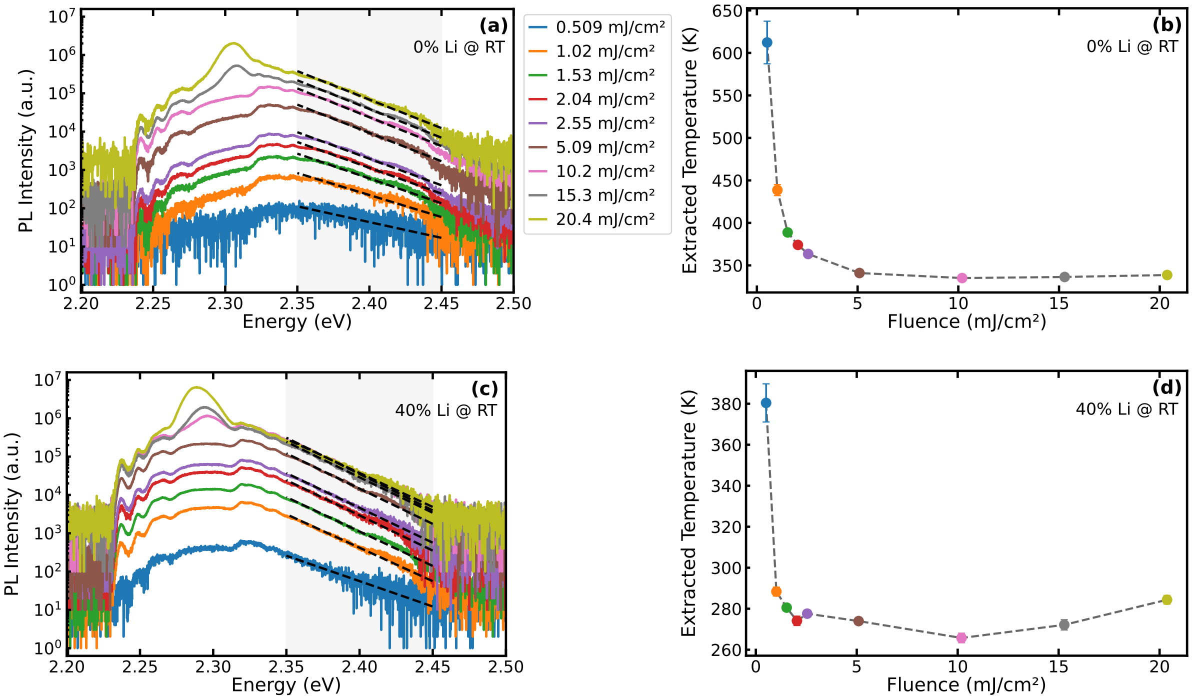

Figure S2 High-energy tail analysis of the RT high-fluence PL spectra for undoped (0% Li) and Li-doped (40% Li) NCs. Panels **(a)** and **(c)** display the high-energy PL tails plotted as $\ln(I - C)$ versus $\Delta E = E - E_g$ within the shaded fitting region. The dashed lines correspond to Boltzmann-tail fits, for which the slope $m = -1/(k_B T)$ yields the effective carrier temperature. Panels **(b)** and **(d)** show the extracted carrier temperatures as a function of excitation fluence for the 0% and 40% Li samples, respectively. In both cases, the fitted slopes become progressively less negative with increasing fluence, corresponding to an increase in the effective carrier temperature. This trend is consistent with photoinduced carrier heating at room temperature. The error bars reflect uncertainties associated with the high-energy tail fits. Legend is shown in panel **(a)**.

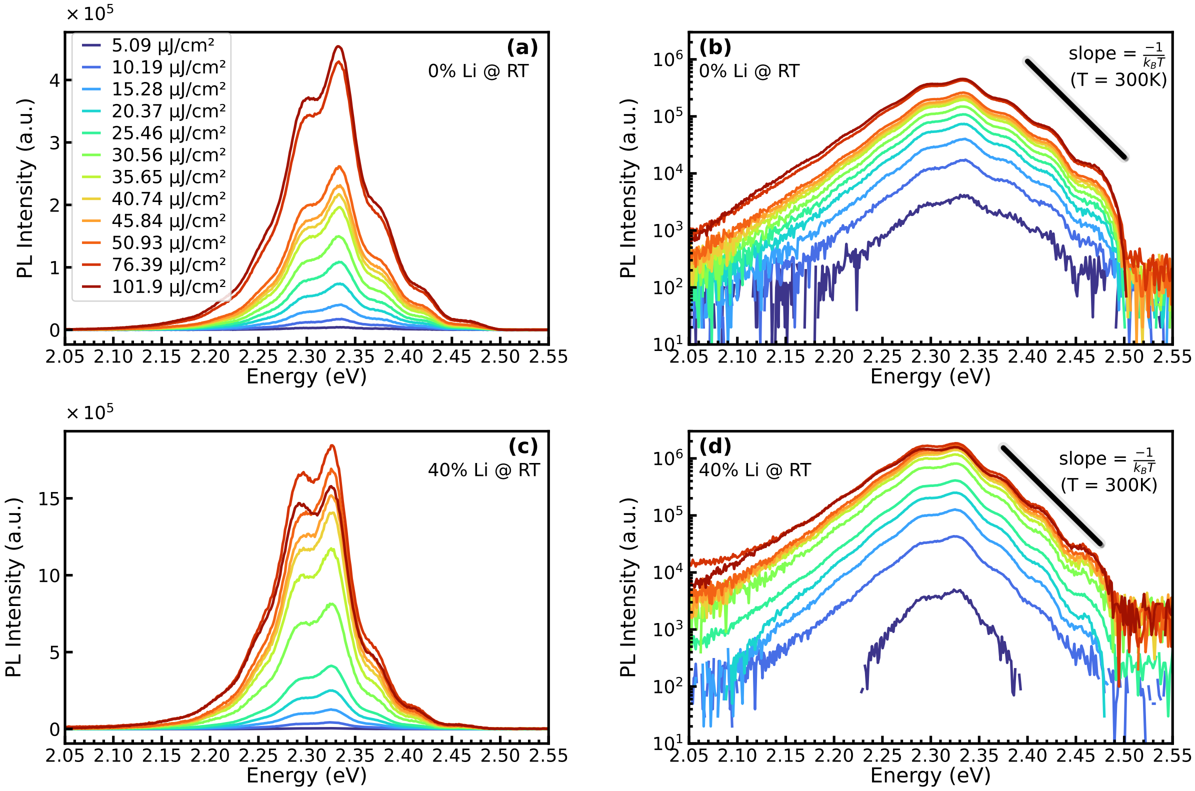

Figure S3 Low-fluence PL at RT under excitation of 800 nm for undoped (0% Li) and Li-doped (40% Li) $\mathrm{CsPbBr_3}$ NCs. Panels **(a)** and **(b)** show the 0% Li spectra on linear and semi-logarithmic intensity scales, respectively; panels **(c)** and **(d)** show the corresponding 40% Li data. The legend indicates the incident fluence in $\mu\mathrm{J/cm^2}$. On the semi-log plots, the high-energy PL tail is approximately exponential in energy and is compared to a guideline with slope $-1/(k_BT)$ expected for a Boltzmann-distributed exciton population. For the 40% Li sample, the high-energy tail closely follows the $T \approx 300\,\mathrm{K}$ guideline, consistent with thermalization at RT, whereas for the 0% Li sample the tail is slightly shallower, corresponding to an effective temperature somewhat higher than 300 K, indicative of additional broadening and/or residual hot-carrier contributions. For the legend, refer to panel **(a)**.

gain-like effects, and nonlinear population redistribution are minimal. As such, these measurements provide a baseline view of the excitonic manifold and its fluence dependence before the onset of saturation and high-density effects, enabling a direct comparison with the high-fluence behavior.

As in the high-fluence measurements, the semi-logarithmic spectra exhibit an approximately exponential high-energy tail, consistent with a Boltzmann-like distribution. However, in the low-fluence regime, the tail behavior primarily reflects a near-equilibrium distribution with minimal photoinduced hot-carrier heating and reduced nonlinear population redistribution, providing a low-density reference for the carrier thermalization trends observed at higher fluences.

We also note the presence of high-energy features/peaks in the region where the Boltzmann-tail approximation is applied, as displayed in **Fig. S3**. We believe these features might be related to the fine structure of the excitonic states arising from conduction-band splitting due to electron–hole exchange interactions, which split the exciton into a dark singlet state and bright triplet states, as discussed by Becker *et al.*[1] Subsequent Rashba-type effects can further modify this structure and shift the relative energies of the bright states. We therefore attribute the observed high-energy

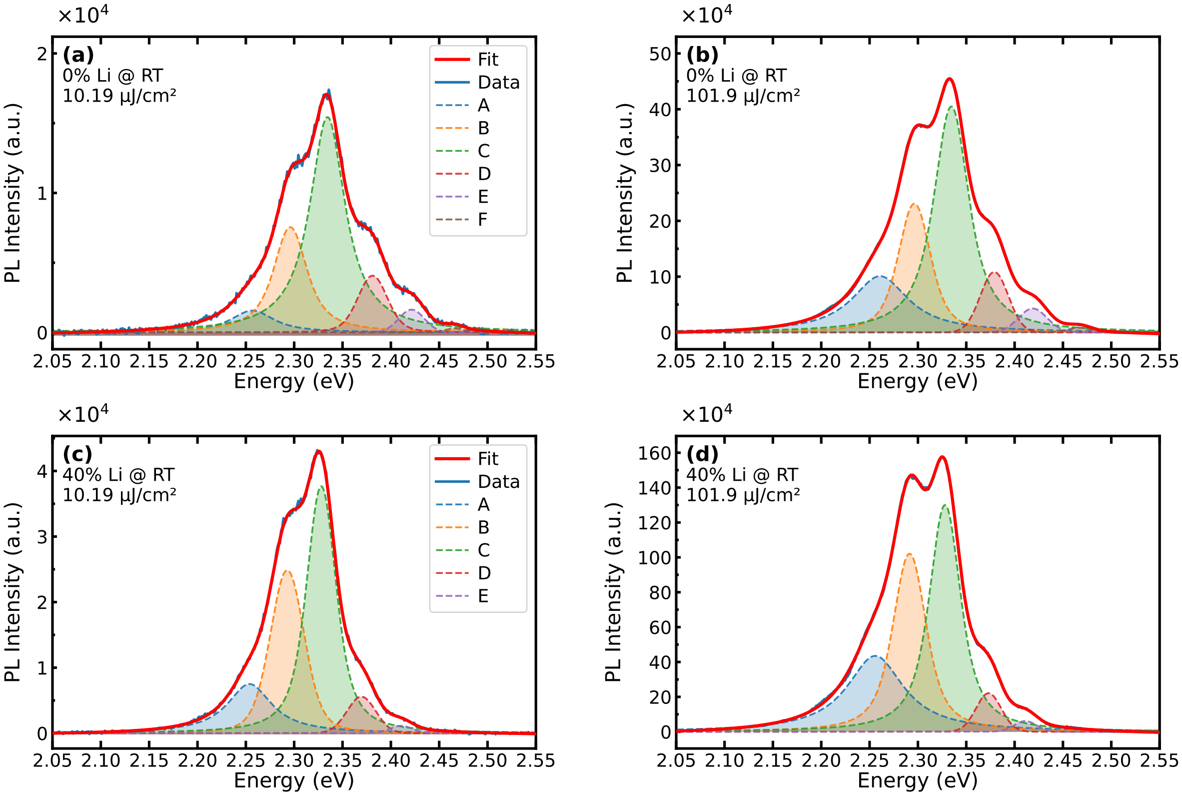

Figure S4 PL spectra at RT and Voigt-fit components for 0% and 40% Li-doped $CsPbBr_3$ NCs under low excitation fluence. Panels **(a)** and **(c)** show the fitted PL spectra at $10.19\,\mu\mathrm{J/cm^2}$ for 0% and 40% Li, respectively, while panels **(b)** and **(d)** show the corresponding fits at $101.9\,\mu\mathrm{J/cm^2}$. In each panel, the measured PL spectrum is plotted together with the total Voigt fit and its individual spectral components, which define the peak positions and relative weights used throughout the analysis. The legend entries for 0% and 40% Li are shown in panels **(a)** and **(c)**, respectively.

spectral features above the band edge to emission from these triplet excitonic states.

To enable a quantitative comparison of individual excitonic contributions as a function of excitation density, we next analyze the fluence dependence of the resolved PL peaks. An immediate observation is that the 40% Li-doped sample exhibits approximately an order-of-magnitude enhancement in PL intensity across the low-fluence range. This enhancement mirrors the trend observed at higher fluence and supports the interpretation that Li incorporation primarily passivates nonradiative recombination pathways rather than modifying the intrinsic excitonic structure. The persistence of this enhancement from the low- to high-fluence regimes indicates that Li-induced passivation is effective across a broad range of excitation densities.

To investigate the two-photon absorption nature of the PL, we labeled the PL peaks and then fit the spectra with Voigt profiles using the same fitting model to extract the peak intensity and energy. Peaks are labeled from left to right with alphabetic labels (A, B, . . .). **Fig. S4** displays example fitting components and peak assignments for the low-fluence PL spectra at RT under $10.19\,\mu\mathrm{J/cm^2}$ and $101.9\,\mu\mathrm{J/cm^2}$ excitation. We should note that peak F near 2.46 eV is not considered in the comparative analysis between 0% and 40% Li due to its low intensity and the difficulty of reliably identifying it in the 40% Li fits.

Peak intensities, extracted from the peak heights of the Voigt-profile fits, are plotted as a function

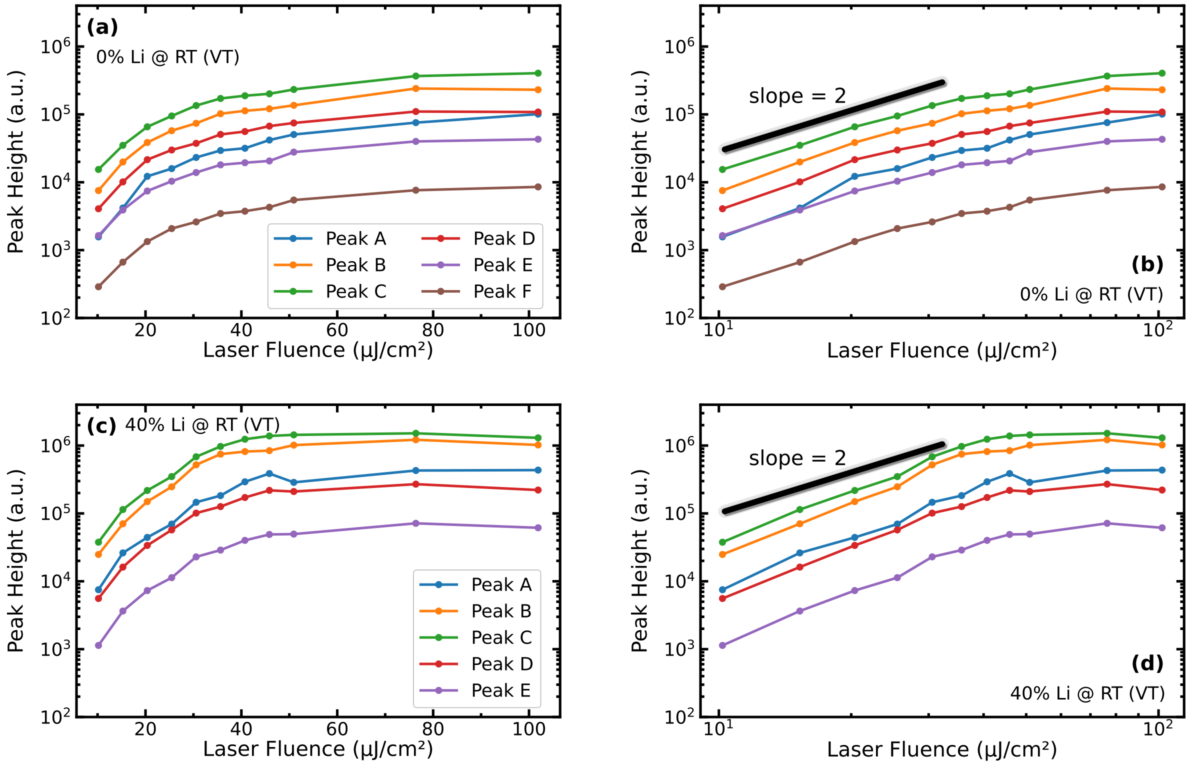

Figure S5 Peak intensity versus fluence, extracted as peak heights from Voigt-profile fits to the PL data in **Fig. S3**. Panels **(a, c)** show the peak intensities versus fluence for 0% and 40% Li doped sample on semi-log scales, while panels **(b, d)** present the peak intensities versus excitation fluence on a log-log scale. A reference line with slope 2 (black) indicates two-photon absorption at lower fluence values. The legend entries for 0% and 40% Li are shown in panels **(a)** and **(c)**, respectively. VT refers to the data from Virginia Tech, in the legends.

of excitation fluence in **Fig. S3**. In contrast to the high-fluence data, where saturation occurs only at fluences of several mJ/cm^2, the low-fluence measurements exhibit saturation at substantially lower fluences of 40-50 μJ/cm^2. This difference highlights the role of excitation conditions and repetition rate in governing carrier accumulation and saturation behavior.

Despite the substantially lower excitation fluence used in the Virginia Tech measurements (maximum fluence $\sim$0.1 mJ/cm^2), the measured PL intensities are approximately three orders of magnitude higher than those obtained in the NHMFL experiments (minimum fluence $\sim$0.5 mJ/cm^2). This difference arises primarily from experimental factors rather than intrinsic sample properties, because two different excitation sources were used, resulting in different laser fluence regimes. This difference primarily reflects the much higher repetition rate used in the Virginia Tech measurements (80 MHz) compared to the 1 kHz system at NHMFL, which leads to increased average excitation density and carrier accumulation, thereby enhancing the observed PL intensity.

We should note that the laser spot size at NHMFL was estimated visually, resulting in an uncertainty of approximately ±15–20%. Using standard error propagation, this corresponds to an estimated systematic uncertainty of ±15–20% for the low-fluence range ($(5.09 \pm 0.89)\,\mu$J/cm^2 to $(101.90 \pm 17.83)\,\mu$J/cm^2) and ±20–30% for the high-fluence range ((0.51 ± 0.13) mJ/cm^2 to (20.37 ± 5.09) mJ/cm^2).

The initial low-fluence measurements were performed from June 18 to July 1, 2024, followed by high-fluence measurements at the National High Magnetic Field Laboratory from July 20 to August 4, 2024. A second low-fluence data set was collected from August 27 to September 3, 2025. The consistent PL emission across these measurements demonstrates the exceptional long-term robustness of the samples.

S4 Two-Photon Absorption

We analyzed the power-law dependence of our PL peak intensity in the low-fluence regime to identify the dominant excitation mechanism under our 800 nm pumping conditions. For each specific emission peak, we performed a linear fit to $\log I$ versus $\log F$ (where F is the excitation fluence), where saturation effects are minimal. The resulting power-law exponents are summarized in **Fig. S6**. Across both high-fluence (NHMFL) and low-fluence (Virginia Tech) datasets, the extracted slopes indicate a value of approximately 2, consistent with two-photon absorption (TPA) dominating the carrier-generation process.

This behavior is also directly visualized in the fluence-dependent intensity plots shown in **Fig. S5**. In the log–log representations [panels **(b, d)**], the low-fluence PL intensities follow a trend with a slope of 2 (black line), providing an independent and graphical confirmation of the TPA scaling. Together, the quantitative slope analysis and the log–log intensity trends demonstrate that the observed RT emission under 800 nm excitation originates from a nonlinear two-photon absorption process.

S5 Peak Energies

We note that a small but systematic redshift of approximately 20 meV is observed for the Li-doped (40% Li) NCs relative to the undoped (0% Li) samples across *both* NHMFL and Virginia Tech data sets, as seen in **Fig. S7**. Importantly, this offset is essentially constant over the entire excitation-fluence range and does not evolve with fluence.

The magnitude of this redshift is comparable to the expected confinement-energy scale for NCs in the weak-confinement regime and to the fitting uncertainty, and therefore does not indicate excitation-induced bandgap renormalization or a modification of the intrinsic electronic structure. Instead, it is consistent with a modest Li-induced increase in effective NC size and/or changes in dielectric screening, as discussed in **Sec. S1** of the Supplementary Information and in the main text.

References

[1] M. A. Becker, R. Vaxenburg, G. Nedelcu, P. C. Sercel, A. Shabaev, M. J. Mehl, J. G. Michopoulos, S. G. Lambrakos, N. Bernstein, J. L. Lyons *et al.*, *Nature*, 2018, **553**, 189–193.

[2] X. Li, Y. Wu, S. Zhang, B. Cai, Y. Gu, J. Song and H. Zeng, *Advanced Functional Materials*, 2016, **26**, 2435–2445.

[3] C. C. Stoumpos, C. D. Malliakas, J. A. Peters, Z. Liu, M. Sebastian, J. Im, T. C. Chasapis, A. C. Wibowo, D. Y. Chung, A. J. Freeman *et al.*, *Crystal growth & design*, 2013, **13**, 2722–2727.

[4] I. Pashuk, N. Pidzyrailo and M. Matsko, *Sov. Phys. Solid State*, 1981, **23**, 1263.

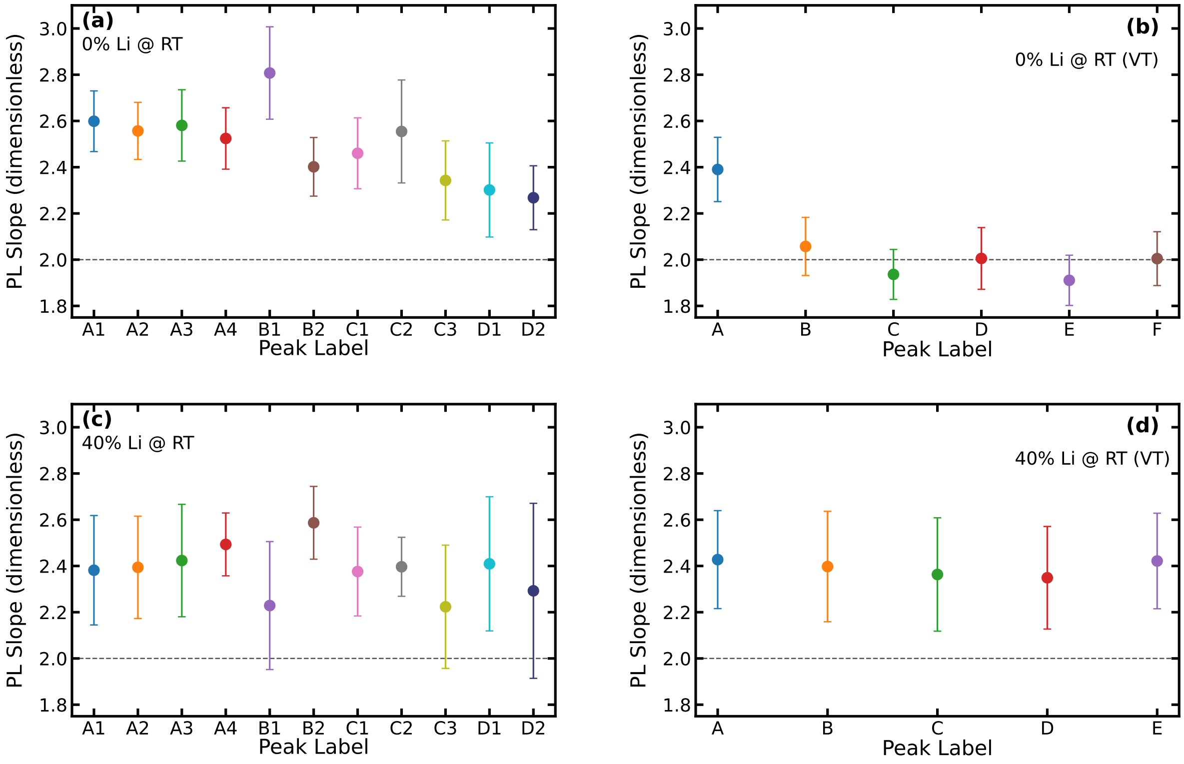

Figure S6 Power-law exponents extracted from the log–log fits of our observed PL peak intensity versus excitation fluence for undoped (0% Li) and Li-doped (40% Li) NCs at RT. Panels **(a, c)** show the slope distributions obtained from the NHMFL measurements (high-fluence), while panels **(b, d)** present the corresponding Virginia Tech data (low-fluence). For each peak, the fitted exponent is shown separately. In all datasets, the slopes suggest a value of ∼ 2, consistent with a TPA process governing the excitation dynamics at low-fluence. In the legends, VT refers to Virginia Tech.

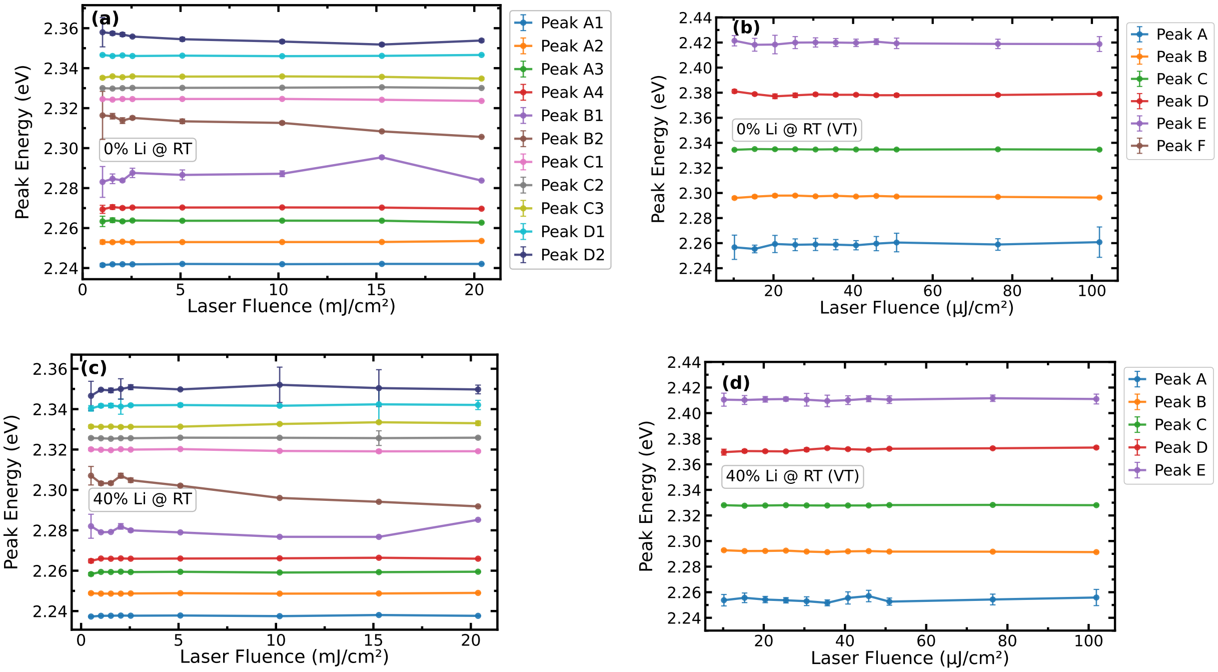

Figure S7 Fits to the peak energies as a function of excitation fluence for undoped (0% Li) and Li-doped (40% Li) NCs at RT. Panels **(a, b)** present the NHMFL (high-fluence) data for 0% and 40% Li, and panels **(c, d)** present the corresponding Virginia Tech measurements (low-fluence). Each curve corresponds to an individual PL peak; visible error bars denote the standard deviation of the fitted peak centers. Across both data sets, the peak energies are essentially independent of excitation fluence. A small but systematic redshift of approximately 20 meV is observed for the 40% Li sample relative to the undoped sample, which remains constant with fluence and is consistent with weak-confinement effects rather than excitation-induced bandgap renormalization. In the legends, VT refers to Virginia Tech. For the panel (c) legend, refer to panel (a).

[5] Z. Yang, A. Surrente, K. Galkowski, A. Miyata, O. Portugall, R. Sutton, A. Haghighirad, H. Snaith, D. Maude, P. Plochocka *et al.*, *ACS Energy letters*, 2017, **2**, 1621–1627.

[6] F. A. Rodríguez Ortiz, B. Zhao, J.-R. Wen, J. E. Yim, G. Bauer, A. Champ and M. T. Sheldon, *The Journal of Physical Chemistry C*, 2023, **127**, 14812–14821.

[7] M. Baranowski and P. Plochocka, *Advanced Energy Materials*, 2020, **10**, 1903659.

[8] P. Umari, E. Mosconi and F. De Angelis, *Scientific reports*, 2014, **4**, 4467.

[9] F. Brivio, K. T. Butler, A. Walsh and M. Van Schilfgaarde, *Physical Review B*, 2014, **89**, 155204.

[10] A. Miyata, A. Mitioglu, P. Plochocka, O. Portugall, J. T.-W. Wang, S. D. Stranks, H. J. Snaith and R. J. Nicholas, *Nature Physics*, 2015, **11**, 582–587.

[11] J.-H. Cha, J. H. Han, W. Yin, C. Park, Y. Park, T. K. Ahn, J. H. Cho and D.-Y. Jung, *The journal of physical chemistry letters*, 2017, **8**, 565–570.

[12] D. Fröhlich, K. Heidrich, H. Künzel, G. Trendel and J. Treusch, *Journal of Luminescence*, 1979, **18**, 385–388.

[13] M. Sebastian, J. Peters, C. Stoumpos, J. Im, S. Kostina, Z. Liu, M. Kanatzidis, A. Freeman and B. Wessels, *Physical Review B*, 2015, **92**, 235210.

[14] L. Protesescu, S. Yakunin, M. I. Bodnarchuk, F. Krieg, R. Caputo, C. H. Hendon, R. X. Yang, A. Walsh and M. V. Kovalenko, *Nano letters*, 2015, **15**, 3692–3696.

[15] G. R. Yettapu, D. Talukdar, S. Sarkar, A. Swarnkar, A. Nag, P. Ghosh and P. Mandal, *Nano letters*, 2016, **16**, 4838–4848.